ADVANCED ENGINEERING MATERIALS

DOI: 10.1002/adem.201500548

Ultra-Fast One-Step Fabrication of Cu_2Se Thermoelectric Legs With Ni–Al Electrodes by Plasma-Activated Reactive Sintering Technique**

By *Linchun Wu, Xianli Su, Yonggao Yan,* Ctirad Uher* and *Xinfeng Tang**

In this study, a novel ultra-fast method is developed to fabricate thermoelectric (TE) legs and electrodes from raw elemental materials in just one-step plasma-activated reactive sintering (PARS) process. We have demonstrated this approach with TE legs made of Cu_2Se and the Ni–Al multiphase composite electrode. The obtained Cu_2Se material shows a maximum ZT value of 0.9 at 773 K. The lowest specific interfacial resistivity of the as-prepared Cu_2Se/electrode junction is about 30 $m\Omega\,cm^2$ at room temperature. The interfacial bonding strength is about 10 MPa. This method shows great prospects for large-scale, low-cost, and rapid fabrication of thermoelectric modules.

1. Introduction

Thermoelectric (TE) materials are functional materials which can directly covert heat into electricity and vice versa. Thermoelectric power generation technologies have a commercialization potential in the fields of solar photovoltaics, thermoelectric hybrid generators,[1] and the recovery of waste industrial heat[2] including that of cars and trucks[3] and converting it to electricity. Large-scale applications of the TE technology would make a meaningful contribution to replacing fossil fuel-based industrial processes. However, the current cost of TE-based power generation is much higher than the electricity generated via fossil fuel-fired plants, and the thermoelectricity is only attractive in niche areas of applications such as deep-space explorations and for operations in remote areas where the exceptional reliability of thermoelectric devices is a distinct advantage. The key factor to reduce the cost of the TE technology is to develop novel, more efficient, and low cost TE materials and implement simple, reliable, and economical fabrication processes for thermoelectric modules.

The conversion efficiency of TE materials depends on the temperature of the hot and cold junctions which determines the Carnot efficiency, and on the material's dimensionless figure of merit ZT, defined as $ZT = \alpha^2\sigma T/(\kappa_L + \kappa_e)$, where α, σ, κ_L, κ_e, and T refer to the Seebeck coefficient, the electrical conductivity, the lattice thermal conductivity, the carrier thermal conductivity, and the absolute temperature, respectively. In addition, a well-functioning TE module requires efficient heat exchangers which couple the TE elements to the hot and cold reservoirs. Since all large-scale applications of thermoelectricity must be cost effective, the synthesis of TE materials and the module fabrication must be simple and inexpensive.

Currently, the fabrication of TE devices is an assembly process from materials to a module. TE materials are synthesized in advance by one of the techniques appropriate for that particular class of materials which may include melting and solidification methods,[4] solid state reaction,[5] levitation melting,[6] mechanical alloying,[7] melt spinning,[8] arc melting,[9] and others. Since not every synthesis process results in a well-densified material, the grown ingots or pellets are ground into a powder and either hot-pressed (HP) or spark plasma sintered (SPS) to the near theoretical density of the material. After cutting the thermoelectric legs into the desired shape and size, reliable low resistance electrical connections must be made between the TE legs and the electrodes by either soldering,[10] brazing,[11] or spraying.[12] Recently, SPS[13] and HP[14] were used to achieve the densification and electrode application in a one-step operation, however, it was necessary to prepare the TE powder

[*] *Prof. X. Tang, Dr. Y. Yan, Dr. L. Wu, Dr. X. Su*
State Key Laboratory of Advanced Technology for Materials Synthesis and Processing, Wuhan University of Technology, Wuhan 430070, China
E-mail: tangxf@whut.edu.cn; yanyonggao@whut.edu.cn
Prof. C. Uher
Department of Physics, University of Michigan, Ann Arbor, Michigan 48109, USA

[**] *We wish to acknowledge support from the National Basic Research Program of China (973 program) under project 2013CB632502 and the Natural Science Foundation of China (Grant Nos. 51401153, 51402222, and 51521001). (Supporting Information is available online from Wiley Online Library or from the author).*

through a complex process in advance. To sum up, the current assembly techniques of TE modules are hampered by a complex assembly process, high energy cost, and long preparation times. Moreover, the high-temperature gradient and associated mechanical shock during the high-temperature soldering/brazing/spraying process has usually a detrimental effect on TE properties of the material. While the above processes and approaches are usually adequate in the laboratory setting where one deals with assembling a few TE couples, it is difficult to export and adopt these processes for large-scale fabrication and guarantee the consistency in the composition and homogeneity of the TE material and the mechanical robustness of the module. The major problem is that the synthesis of TE materials and the application of electrodes is not a simple and facile one-step process.

To overcome these drawbacks, we have developed an ultra-fast fabrication method, called plasma-activated reactive sintering (PARS) that, in one-step, achieves the fabrication of TE legs from raw elemental materials together with the formation of electrodes and an appropriate densification of the entire assembly. To demonstrate the fabrication technique, we have chosen a low-cost Cu_2Se TE material and successfully fabricated Cu_2Se TE legs and electrodes by the PARS method starting from elemental Cu, Se, Ni, and Al powders. The ultra-fast phase transition process that Cu_2Se undergoes, the resulting microstructure, and TE transport properties of Cu_2Se legs have been investigated as a function of the sintering temperature with the aid of in situ temperature detection. The ZT value of the PARS-synthesized Cu_2Se is comparable with the same material prepared by melting and sintering.[15] The microstructure of the electrodes and the interface between Cu_2Se and the electrode were also characterized and evaluated. The lowest specific interfacial resistivity of the Cu_2Se/electrode interface is about 30 $\mu\Omega\,cm^2$ at room temperature. The interfacial bonding strength is about 10 MPa, comparable to the shear strength of Cu_2Se. Compared with the traditional TE module fabrication methods, the one-step PARS method greatly shortens the preparation period and simplifies the preparation process. The high-efficiency low-cost PARS method will also be applicable for other TE materials that can be prepared by the combustion synthesis and is suitable for large-scale commercial fabrication of TE modules.

2. Experimental Section

High-purity Cu (4 N, 600 mesh), Se (4 N, 200 mesh), Ni (2.5 N, 200 mesh), and Al (4 N, 100 mesh) powders were weighed and mixed according to the nominal composition of Cu_2Se and $NiAl_3$. Mixed powders of Ni–Al, respectively, of Cu–Se, were poured into the graphite die as separate layers, as depicted in Figure 1a, and then the graphite die was subjected to the PARS process (Ed-PAS-111, Japan) with a pressure of 35 MPa holding for 5 min at different sintering temperatures of 500, 550, and 650 °C, respectively. The dense columnar

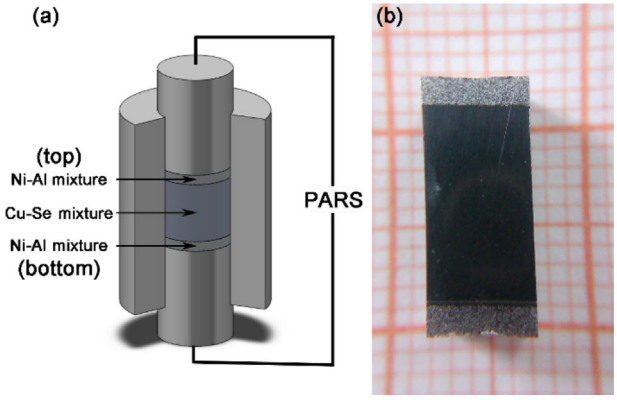

Fig. 1. (a) Illustration of the one-step PARS method (b) photograph of the sintered thermoelectric leg.

bulk samples with electrodes at both ends were obtained, with the thickness of the electrode layers of about 1 mm and the thickness of the TE material of about 10 mm. A rectangular-bar with dimensions of $5 \times 5 \times 12\,mm^3$ (Figure 1b) was cut from the columnar bulk along the axial direction, and its electrical conductivity, Seebeck coefficient, and characteristics of the Cu_2Se–electrode interface were measured. To characterize the properties of Cu_2Se, rectangular sheets of $8 \times 8 \times 1.5\,mm^3$ and $3 \times 8 \times 1\,mm^3$ were cut from the TE material for thermal diffusivity and Hall-effect measurements, respectively.

The phase composition of the samples is characterized by powder X-ray diffraction (XRD, PRO-PANalytical Empyrean, Cu $K_{\alpha,}$ Netherlands). The morphology and composition are determined by field emission scanning electron microscopy (FESEM, Hitachi SU-8020, Japan), energy dispersive spectrum (EDS), and electron probe microanalysis (EPMA, JXA-8230, JEOL, Japan) with the wavelength dispersive spectrum (WDS) analysis. The electrical conductivity (σ) and the Seebeck coefficient (α) are measured simultaneously by a standard four-probe method with an Ulvac-Riko ZEM-3 system. The thermal diffusivity (D) is obtained by the laser flash method (LFA-457, Netzsch, Germany) and the specific heat (C_p) is measured by a differential scanning calorimeter (DSC Q20, TA Instrument, USA). The density (d) is measured by the Archimedes method and the relative density of bulk Cu_2Se samples was higher than 98%. The thermal conductivity was calculated according to the relationship $\kappa = DC_pd$. All measurements were performed in the temperature range from 300 to 773 K. Uncertainties in the electrical conductivity, Seebeck coefficient, and thermal conductivity were within 5, 2, and 5%, respectively, primarily originating from sample dimension measurements. Room-temperature Hall-effect data were collected using a physical properties measurement system (PPMS-9, Quantum Design, USA). The carrier concentration (p) and the Hall mobility (μ_H) were determined by $p = 1/eR_H$ and $\mu_H = \sigma R_H$. The electrical contact resistance of the Cu_2Se/electrode interface was measured by a four-probe method using a home-made apparatus (see Supporting Information for more details, Figure S1). The shear strength

tests were carried out at room temperature on an MTS universal test machine (QJ210A-500N, MTS, China) with a crosshead speed of 0.2 mm min^{-1}.

3. Results and Discussion

3.1. Cu_2Se Material

3.1.1. Phase Composition and Reaction Mechanism of Cu_2Se

Figure 2 displays the powder XRD patterns of the Cu_2Se thermoelectric material after PARS at various sintering temperatures, PARS-500, PARS-550, and PARS-650 represent the samples which were sintered at 500, 550, and 650 °C, respectively. It is evident that almost all diffraction peaks correspond well with the standard pattern for Cu_2Se (JCPDS #47-1448), indicating that all samples are perfect single-phase structures. In order to probe differences in the chemical composition of the samples sintered at different temperatures, Figure 3 shows the DSC curves of Cu_2Se after PARS at various sintering temperatures. As depicted in the picture, the α-Cu_2Se to β-Cu_2Se phase-transition temperature shows a shift from 132 to 127 °C with the increasing PARS temperature. As reported in the literature,[16] the α-Cu_2Se to β-Cu_2Se phase-transition temperature decreases with the reduction in the content of Cu. Herein, a greater Cu deficiency is found with the increase of the PARS temperature. The high-temperature β-Cu_2Se is a fast ionic conductor, where the Cu^+ ions easily move on the sub-lattice formed by Se. It is supposed that the copper deficiency originates from the mobility of the Cu^+ ion along the PARS current direction. As the sintering temperature increases, the larger PARS current leads to a greater number of mobile Cu^+ ions along the current direction,[17] resulting in a more severe deficiency of copper in the Cu_2Se material.

In order to investigate the formation mechanism of Cu_2Se during the PARS process, we used three thermocouples to measure the temperature of the sample at different positions, as depicted in the right-hand side inset of Figure 4b. Figure 4a is a photograph of the measurement setup. Figure 4b shows the time-dependent temperature and the piston displacement during the PARS process. As the temperature is ramped up, after about 25 s, the bottom and the center of the sample show a near simultaneous temperature jump, more clearly displayed in the inset of Figure 4b. To clarify the origin of the temperature jump, we measured in a separate run the phase composition of the sample cooled quickly from the temperature just above where the jump took place and the sample turned out to be a perfect single-phase Cu_2Se. Thus, we ascribe the temperature jump to an instant exothermic heat released in the combustion synthesis of Cu_2Se. It is noteworthy that the piston's displacement of the spark plasma sintering system also shows a jump simultaneously with the temperature jump owing to the volume shrinkage during the reaction process. The above results show that the Cu_2Se phase is obtained below 200 °C via a combustion synthesis of powders of Cu and Se and the densification of the TE material as well as the electrode is completed later during the sintering stage at higher temperatures.

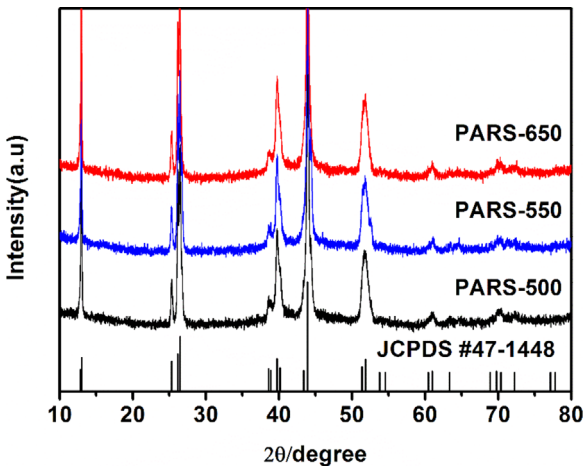

Fig. 2. Powder XRD patterns of Cu_2Se after PARS carried out at different sintering temperatures.

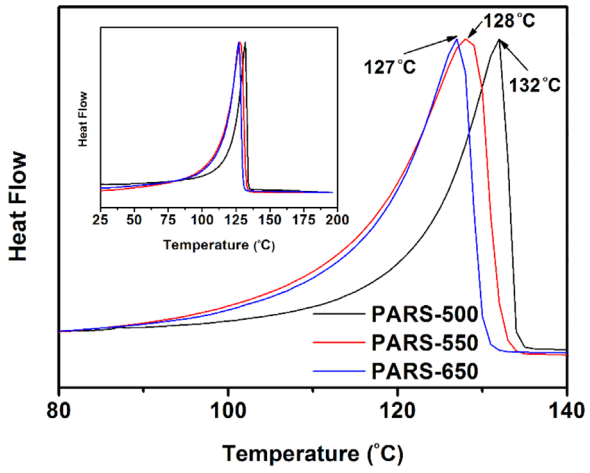

Fig. 3. DSC curves of Cu_2Se after PARS carried out at different sintering temperatures.

3.1.2. Microstructure of Cu_2Se

Figure 5 shows FESEM images of the fracture surface of Cu_2Se fabricated by the one-step PARS method. As shown in the figure, with the increase of the PARS temperature, the grain size increases notably (Figure 5a, c), and more pores with the size distribution of several nanometers to hundreds of nanometers are found (Figure 5b, d). We suppose that the nanopores originate from the combustion process, as noted in the literature.[18]

3.1.3. Thermoelectric Properties of Cu_2Se

To further study the impact of PARS temperature on TE properties, we measured and evaluated transport properties of samples sintered at various temperatures. Figure 6a shows the temperature-dependent electrical conductivity. For all samples, the electrical conductivity decreases with the increasing temperature (showing the behavior of a

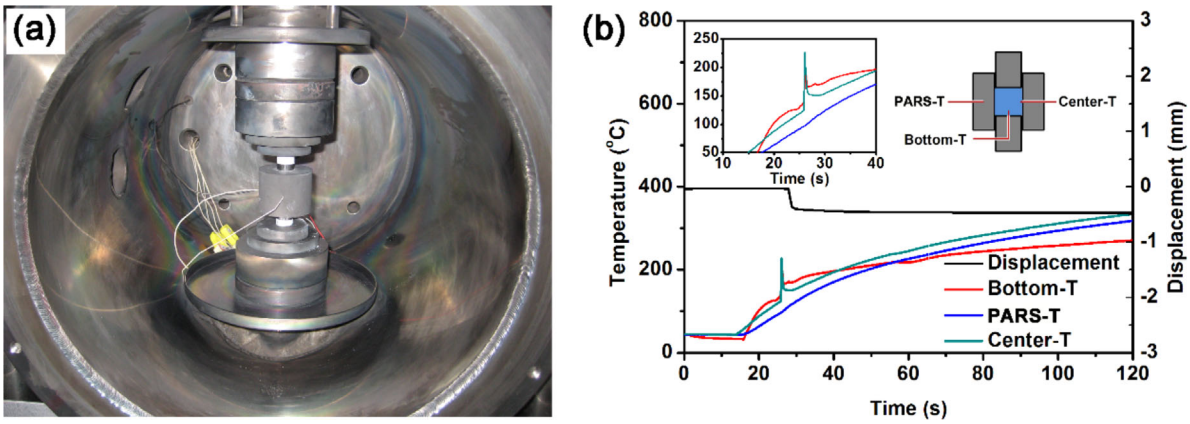

Fig. 4. (a) Photograph showing the setup to measure the PARS temperature, (b) time dependence of the PARS temperature and the piston displacement during the PARS process.

degenerate semiconductor) except for a point at about 400 K which indicates a phase transition in Cu_2Se. The decrease in the electrical conductivity can be ascribed to intensified lattice scattering of electrons which reduces their mobility. As the sintering temperature is increased, the electrical conductivity decreases in the entire temperature range. Figure 6b displays the temperature-dependent Seebeck coefficient. For all samples, the Seebeck coefficient is positive at all temperatures which indicates p-type conduction. With the increase of the sintering temperature, the Seebeck coefficient increases slightly.

To clarify the cause of the reduced electrical conductivity, we measured room-temperature Hall coefficient for all samples. The positive Hall coefficient indicates p-type conduction, consistent with measurements of the Seebeck coefficient. As displayed in Figure 7, the resulting carrier concentration shows a slightly increasing trend with the increasing PARS temperature. In contrast, the carrier mobility decreases sharply, which may be the main reason for the diminished electrical conductivity. Combined with the above analysis regarding the Cu deficiency, we can state that as the sintering temperature and the PARS current increase, the copper deficiency increases and this results in more holes being generated in the material.[19] The copper deficiency tends to form copper vacancy and thus results in stronger scattering of charge carriers and, consequently, their reduced mobility. The unusual simultaneous increase in the carrier concentration and the Seebeck coefficient observed here may be related to a change in the carrier scattering mechanism and/or a possible modification of the band structure[20] due to the deficiency of Cu.

Temperature dependence of the thermal conductivity is shown in Figure 8a. The total thermal conductivity κ_t decreases with the increasing temperature of the PARS process. This is primarily due to a decreasing electronic part of the thermal conductivity κ_e which is estimated based on the Wiedemann–Franz law, $\kappa_e = L\sigma T$, where L is the Lorenz number, σ is the electrical conductivity, and T the absolute temperature. Here, we have adopted the value of $L = 2.0 \times 10^8$ V^2 K^{-2} appropriate for degenerate semiconductors.[21] The decreasing κ_e is a consequence of a remarkable decrease in the electrical conductivity upon increasing the PARS temperature. The lattice thermal conductivity $\kappa_L = \kappa_t - \kappa_e$ shows little change with the sintering temperature.

The thermoelectric figure of merit ZT of all the samples is displayed in Figure 8b. At low temperatures, the ZT value is influenced by the phase transition in Cu_2Se taking place near 400 K. As the temperature increases, the figure of merit increases and at high temperatures the figure of merit of all samples becomes similar and attains a value of about 0.9 at 773 K. The ZT performance is comparable with the values reported for samples prepared by the melting and sintering method.[15] Overall, the PARS method shows great advantages over the traditional synthesis approaches in terms of

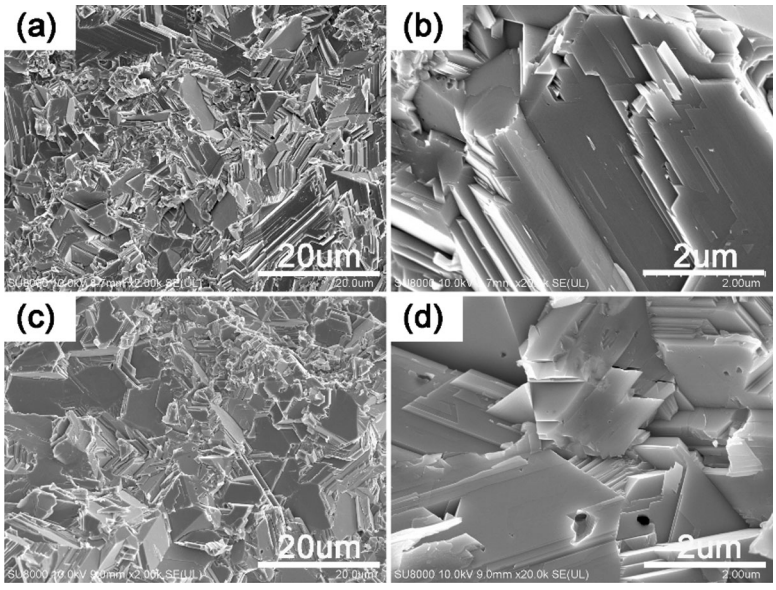

Fig. 5. FESEM images of fracture surfaces of Cu_2Se fabricated by the one-step PARS method. (a, b) PARS-500, (c, d) PARS-650.

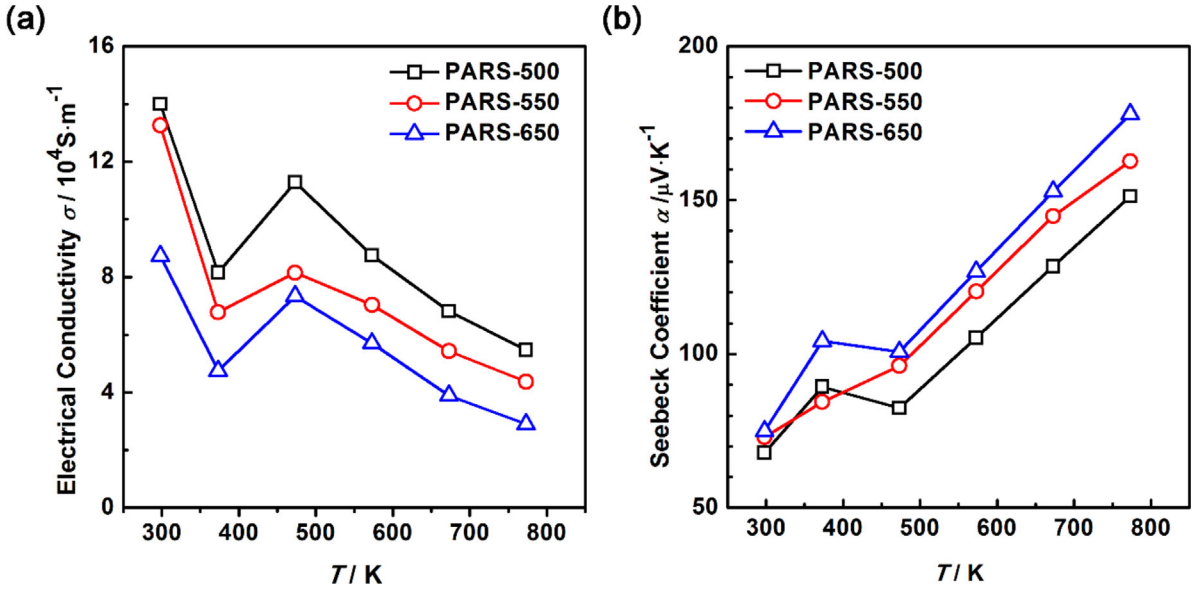

Fig. 6. Temperature dependence of (a) the electrical conductivity and (b) the Seebeck coefficient of Cu_2Se fabricated by the one-step PARS method.

the low-cost and rapid fabrication of TE materials while it maintains the materials' excellent TE performance.

3.2. Cu_2Se/Electrode Interface

3.2.1. Microstructure of the Interface

Figure 9 shows a backscattering electron image (BSI) of the Cu_2Se/electrode interface obtained at different sintering temperatures. (Figure 9a, c, and e show the interface between Cu_2Se and the upper electrode while Figure 9b, d, and f display the interface between Cu_2Se and the lower electrode.) The PARS current flows from the upper to the lower electrode. Results of the chemical composition analysis of the TE material and the electrodes are given in the figures. As depicted in Figure 9a–f, a large white rectangular region in each BSI is the single-phase Cu_2Se. The result is consistent with the XRD analysis. We also note that the chemical composition of this phase changes somewhat from Cu_2Se to $Cu_{1.99}Se$ and to $Cu_{1.98}Se$ as the PARS temperature increases from 500 to 550 °C and to 650 °C. Each chemical composition data point is the average composition value of 10 points taken at different regions of Cu_2Se collected by WDS. Clearly, a copper deficiency is found with the increasing PARS temperature which is in line with the above DSC result.

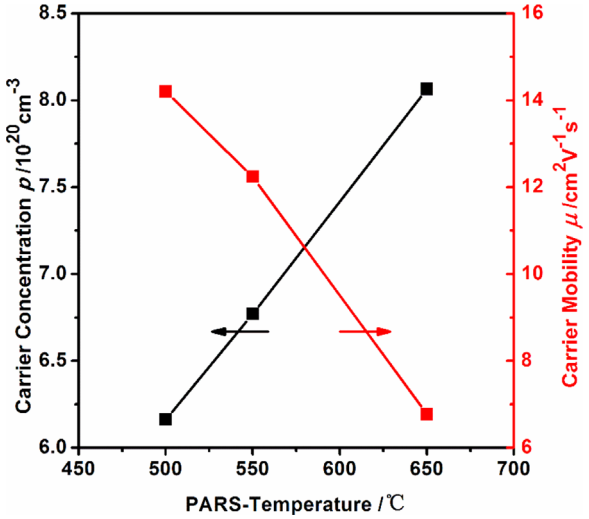

Fig. 7. Variation of room temperature carrier concentration and carrier mobility in Cu_2Se sintered at different PARS temperatures.

As shown in Figure 9, the darker regions with several contrasts are the composite electrodes consisting of Al, $NiAl_3$, Ni_2Al_3, and Ni. It seems that Ni and Al are gradually converted into Ni_2Al_3 and $NiAl_3$ as the sintering temperature increases. Ni, Al, and Ni–Al intermetallic compounds all show a high thermal and electrical conductivity.[22] More importantly, Ni–Al intermetallic compounds have the coefficient of thermal expansion (CTE) close to that of Cu_2Se, i.e., provide an excellent match between the TE material and the electrodes, see Figure S2. The multiphase nature of the electrode provides flexibility to adjust the CTE to match with Cu_2Se and relieve any possible thermal stresses at the interface. It is also interesting to note that the electrode region in contact with Cu_2Se tends to contain several Ni–Al intermetallic compounds. A possible reason is an extra activation energy arising from the heat generated by the combustion synthesis of Cu and Se forming Cu_2Se. Such multicomponent Ni–Al intermetallic layer may help to relieve the thermal stress during the operation and can only serve as a barrier layer on account of its high melting point and good chemical stability.

As the sintering temperature increases, one finds a progressively greater presence of an Al–Cu alloy at the interface (Figure 9d and f). This is especially so at the lower Cu_2Se/electrode interface. There seem to be two factors that may contribute to the formation of the Al–Cu alloy. One is that the Cu^+ ions migrate from the upper to the lower electrode

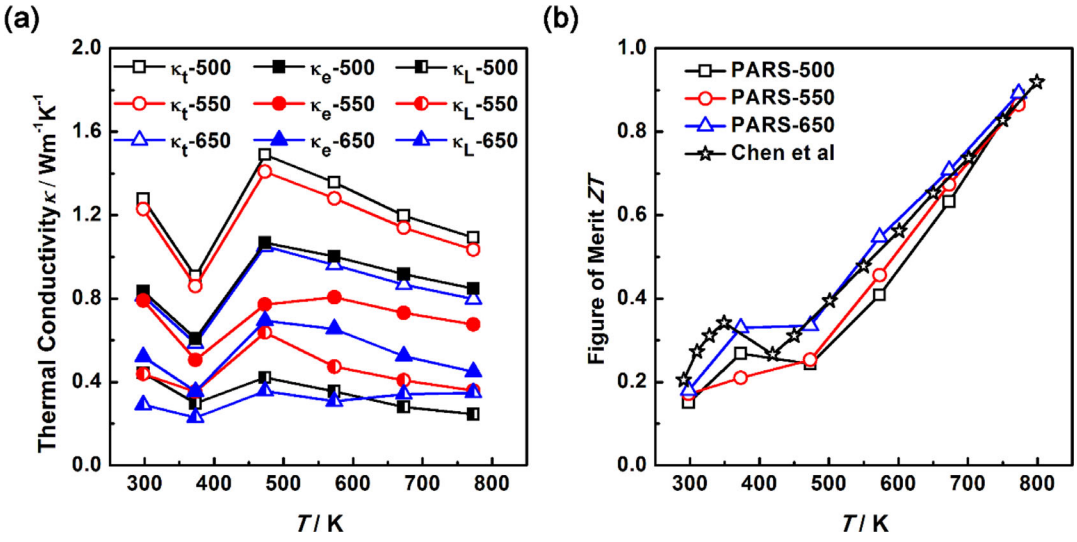

Fig. 8. (a) Temperature dependence of the thermal conductivity and (b) of the thermoelectric figure of merit ZT of Cu_2Se sintered at different temperatures.

driven by the PARS DC current, deposit at the lower interface, and react with the electrode material to form the Al–Cu alloy. The other factor may be a direct reaction between Cu_2Se and aluminum or intermetallic Ni–Al compounds at the interface. At 650 °C, the Al–Cu alloy is found also at the upper interface (Figure 9e), although to a lesser extent than at the lower interface. However, no matter how the Al–Cu alloy forms, at higher sintering temperatures more Cu^+ ions migrate from the upper to the lower electrodes (in the direction of the PARS current) and the elevated temperature enhances the reaction rate between Cu_2Se and the electrodes leading to more Al–Cu alloy formation at interfaces with a consequent influence on the electrical properties, as discussed in the following section.

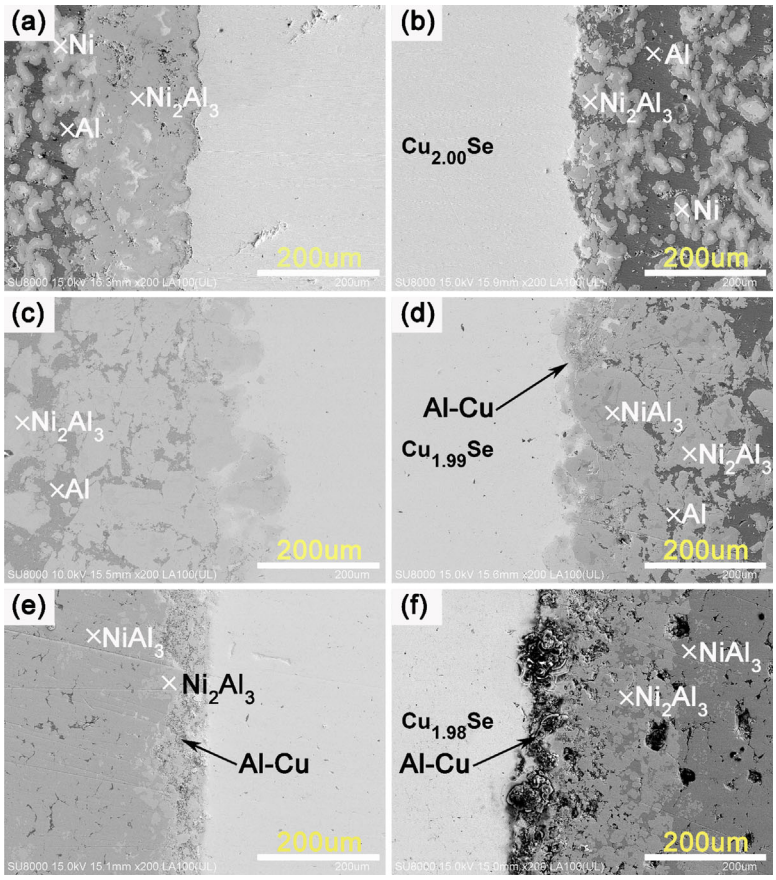

Fig. 9. FESEM micrographs (BSI) and WDS analysis results of the Cu_2Se/electrode interface following PARS processing at (a, b) 500 °C; (c, d) 550 °C; and (e, f) 650 °C. The upper interface is shown in the left-hand column while the lower interface is depicted in the right-hand column.

3.2.2. Electrical Properties of Interfaces between Cu_2Se and Electrodes

The specific interfacial resistivity of samples sintered at different temperatures is shown in Figure 10. The data represent an average value measured on three samples cut from the same sintered columnar bulk sample. It is obvious that the average specific interfacial resistivity increases sharply with the increasing PARS temperature, especially when the PARS temperature is 650 °C. It is also noteworthy that the specific interfacial resistivity of the lower interface is larger than that of the upper interface for all the samples. Relating the specific interfacial resistivity data with BSI images in Figure 9, one may conclude that the increased interfacial resistivity is due to the presence of the Al–Cu alloy at the interface region between Cu_2Se and the electrodes which introduces a lot of cracks (Figure 9f), possibly due to a mismatch between thermal expansion coefficients of Cu_2Se (24×10^{-6} K at 720 K) and the Al–Cu alloy (18×10^{-6} K at 720 K[23]).

ADVANCED ENGINEERING MATERIALS

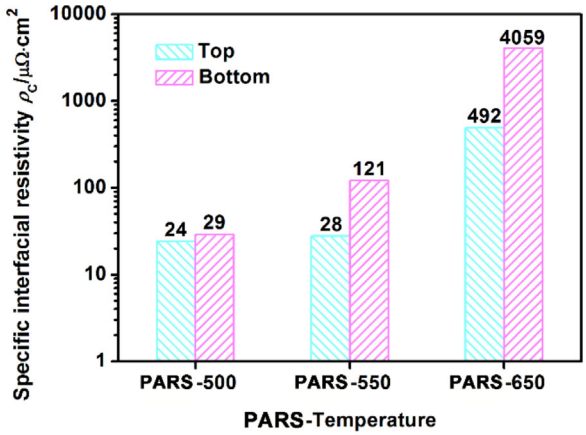

Fig. 10. Comparison of the specific interfacial resistivity among samples sintered at different PARS temperatures.

The effect of the sintering temperature on TE properties and on the specific interfacial resistivity shows that lower sintering temperatures (500 °C) are beneficial for the fabrication of Cu_2Se TE legs. Lower temperatures result in low specific interfacial resistivities while they also preserve excellent TE properties.

3.2.3. Interfacial Bonding Strength

Figure 11 compares the shear strengths of the Cu_2Se–electrode interface prepared by the one-step PARS synthesis (#1) at 500 °C and by a combination of the SHS–PAS processing consisting of Cu_2Se synthesized by the self-propagating high-temperature (SHS) method in advance of attaching electrodes using the plasma-assisted sintering (PAS) (#2). Figure 11 also includes shear strength of Cu_2Se itself (material without electrodes) prepared by the one-step PARS method (#3) and by the SHS–PAS process (#4). The results indicate that the shear strength of the interface and that of Cu_2Se prepared by the one-step PARS method are both comparable to the shear strength of the interface and the shear strength of the Cu_2Se structure prepared by the SHS–PAS method. The respective shear strengths are all comparable with the value of about 10 MPa. The data attest to a very good contact between the Cu_2Se thermoelectric material and the electrodes.

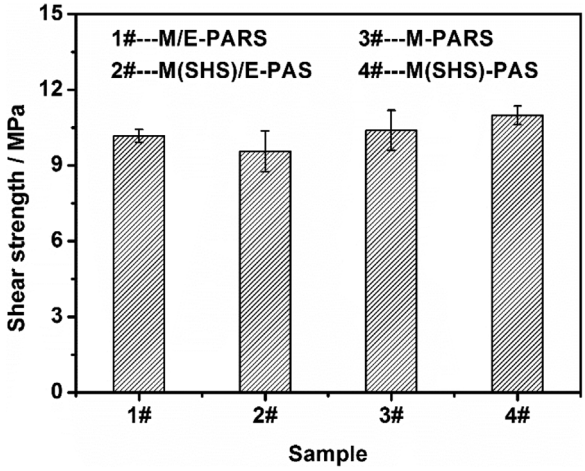

Fig. 11. Shear strength of samples all prepared at 500 °C by different sintering methods designated as follows: M stands for Cu_2Se and E designates an electrode. M (SHS) indicates that Cu_2Se was synthesized by self-propagating high-temperature synthesis. M/E stands for the shear strength at the interface.

4. Conclusions

In this work, we developed an ultra-fast one-step PARS technique to fabricate efficient Cu_2Se thermoelectric legs from elemental raw powders simultaneously with Ni–Al electrodes and we densified the product in a single sintering process. The maximum ZT value of thus prepared Cu_2Se legs is 0.9 at 773 K which compares favorably with Cu_2Se synthesized by the traditional melting and sintering method. The lowest specific interfacial resistivity between Cu_2Se and the electrodes of 30 $\mu\Omega\,cm^2$ is obtained at the lowest sintering temperature of 500 °C. At higher sintering temperatures, migrating Cu^+ ions tend to form Al–Cu alloys at the interfaces which dramatically increase the interface resistance. TE modules using Cu_2Se with Ni–Al electrodes are thus intended for the use at temperatures below 500 °C. The PARS processing can also be applied to the preparation of other TE materials which can be formed by the combustion synthesis process. As n-type TE legs matching the p-type Cu_2Se, one could select Mg_2X, X = Si, Ge, Sn solid solutions, or $CoSb_3$. The PARS synthesis technique offers a low-cost, rapid, and large-scale fabrication of thermoelectric modules.

Article first published online: February 10, 2016
Manuscript Revised: January 15, 2016
Manuscript Received: October 28, 2015

[1] N. Wang, L. Han, H. He, N.-H. Park, K. Koumoto, *Energy Environ. Sci.* **2011**, *4*, 3676.
[2] L. E. Bell, *Science* **2008**, *321*, 1457.
[3] X. Liu, Y. Deng, Z. Li, C. Su, *Energy Convers. Manage.* **2015**, *90*, 121.
[4] a) J. R. Sootsman, J. He, V. P. Dravid, C.-P. Li, C. Uher, M. G. Kanatzidis, *J. Appl. Phys.* **2009**, *105*, 083718. b) Y. Tang, Y. Qiu, L. Xi, X. Shi, W. Zhang, L. Chen, S.-M. Tseng, S.-W. Chen, G. J. Snyder, *Energy Environ. Sci.* **2014**, *7*, 812.
[5] a) W. Liu, X. Tan, K. Yin, H. Liu, X. Tang, J. Shi, Q. Zhang, C. Uher, *Phys. Rev. Lett.* **2012**, *108*, 166601. b) W. Liu, X. Tang, J. Sharp, *J. Phys. D: Appl. Phys.* **2010**, *43*, 085406.
[6] a) C. Fu, T. Zhu, Y. Liu, H. Xie, X. Zhao, *Energy Environ. Sci.* **2015**, *8*, 216. b) C. Yu, T.-J. Zhu, R.-Z. Shi, Y. Zhang, X.-B. Zhao, J. He, *Acta Mater.* **2009**, *57*, 2757.
[7] a) B. Poudel, Q. Hao, Y. Ma, Y. Lan, A. Minnich, B. Yu, X. Yan, D. Wang, A. Muto, D. Vashaee, *Science* **2008**, *320*, 634. b) B. Yu, W. Liu, S. Chen, H. Wang, H. Wang, G. Chen, Z. Ren, *Nano Energy* **2012**, *1*, 472.

[8] a) W. Xie, J. He, H. J. Kang, X. Tang, S. Zhu, M. Laver, S. Wang, J. R. Copley, C. M. Brown, Q. Zhang, *Nano Lett*. **2010**, *10*, 3283. b) Y. Zheng, Q. Zhang, X. Su, H. Xie, S. Shu, T. Chen, G. Tan, Y. Yan, X. Tang, C. Uher, *Adv. Energy Mater*. **2015**, *5*, 1401391.

[9] a) H. Anno, H. Yamada, T. Nakabayashi, M. Hokazono, R. Shirataki, *J. Solid State Chem*. **2012**, *193*, 94. b) G. Joshi, T. Dahal, S. Chen, H. Wang, J. Shiomi, G. Chen, Z. Ren, *Nano Energy* **2013**, *2*, 82.

[10] a) T. Lin, C. Liao, A. T. Wu, *J. Electron. Mater*. **2012**, *41*, 153. b) C. Yang, H. Lai, J. Hwang, T. Chuang, *J. Electron. Mater*. **2013**, *42*, 359.

[11] a) Y. X. Gan, F. W. Dynys, *Mater. Chem. Phys*. **2013**, *138*, 342. b) Y. Zhang, M. Cleary, X. Wang, N. Kempf, L. Schoensee, J. Yang, G. Joshi, L. Meda, *Energy Convers. Manage*. **2015**, *105*, 946.

[12] a) S. Bai, F. Li, T. Wu, X. Yin, X. Shi, L. Chen, *Funct. Mater. Lett*. **2015**, *8*, 1550048. b) H. Mukunoki, O. Fukumasa, S. Sakiyama, *Thin Solid Films* **2002**, *407*, 92.

[13] D. Zhao, H. Geng, L. Chen, *Int. J. Appl. Ceram. Technol*. **2012**, *9*, 733.

[14] D. Kraemer, J. Sui, K. McEnaney, H. Zhao, Q. Jie, Z. Ren, G. Chen, *Energy Environ. Sci*. **2015**, *8*, 1299.

[15] H. Liu, X. Shi, F. Xu, L. Zhang, W. Zhang, L. Chen, Q. Li, C. Uher, T. Day, G. J. Snyder, *Nat. Mater*. **2012**, *11*, 422.

[16] K. Chrissafis, K. Paraskevopoulos, C. Manolikas, *J. Therm. Anal. Calorim*. **2006**, *84*, 195.

[17] D. R. Brown, T. Day, T. Caillat, G. J. Snyder, *J. Electron. Mater*. **2013**, *42*, 2014.

[18] X. Su, F. Fu, Y. Yan, G. Zheng, T. Liang, Q. Zhang, X. Cheng, D. Yang, H. Chi, X. Tang, *Nat. Commun*. **2014**, *5*, 4908.

[19] Y. He, T. Day, T. Zhang, H. Liu, X. Shi, L. Chen, G. J. Snyder, *Adv. Mater*. **2014**, *26*, 3974.

[20] D. Dorfs, T. Härtling, K. Miszta, N. C. Bigall, M. R. Kim, A. Genovese, A. Falqui, M. Povia, L. Manna, *J. Am. Chem. Soc*. **2011**, *133*, 11175.

[21] B. Sales, D. Mandrus, B. Chakoumakos, V. Keppens, J. Thompson, *Phys. Rev. B*. **1997**, *56*, 15081.

[22] G. Dey, *Sadhana* **2003**, *28*, 247.

[23] T.-H. Lee, Y.-J. Lee, K.-T. Park, H.-G. Jeong, J.-H. Lee, *Met. Mater. Int*. **2015**, *21*, 402.

